FOUNDATIONS
ADVANCES

ISSN: 2053-2733
journals.iucr.org/a

Vanishing of the atomic form factor derivatives in non-spherical structural refinement – a key approximation scrutinized in the case of Hirshfeld atom refinement

Laura Midgley, Luc J. Bourhis, Oleg V. Dolomanov, Simon Grabowsky, Florian Kleemiss, Horst Puschmann and Norbert Peyerimhoff

Acta Cryst. (2021). A**77**, 519–533

Acta Cryst A FOUNDATIONS ADVANCES

ISSN 2053-2733

Received 10 June 2021
Accepted 2 September 2021

Edited by P. M. Dominiak, University of Warsaw, Poland

Keywords: quantum crystallography; refinement; non-spherical form factors.

Supporting information: this article has supporting information at journals.iucr.org/a

Vanishing of the atomic form factor derivatives in non-spherical structural refinement – a key approximation scrutinized in the case of Hirshfeld atom refinement

Laura Midgley,[a] Luc J. Bourhis,[b] Oleg V. Dolomanov,[c] Simon Grabowsky,[d] Florian Kleemiss,[d,e] Horst Puschmann[c]* and Norbert Peyerimhoff[a]*

[a]Department of Mathematical Sciences, Durham University, Upper Mountjoy Campus, Stockton Road, Durham, DH1 3LE, United Kingdom, [b]Bruker, 4 Allée Lorentz, Champs-sur-Marne, 77447 Marne-la-Vallée cedex 2, France, [c]OlexSys Ltd, Department of Chemistry, Durham University, South Road, Durham, DH1 3LE, United Kingdom, [d]Departement für Chemie, Biochemie und Pharmazie, Universität Bern, Freiestrasse 3, 3012 Bern, Switzerland, and [e]Fakultät für Chemie und Pharmazie, Universität Regensburg, Universitätsstraße 31, 93053 Regensburg, Germany. *Correspondence e-mail: horst@olexsys.org, norbert.peyerimhoff@durham.ac.uk

When calculating derivatives of structure factors, there is one particular term (the derivatives of the atomic form factors) that will always be zero in the case of tabulated spherical atomic form factors. What happens if the form factors are non-spherical? The assumption that this particular term is very close to zero is generally made in non-spherical refinements (for example, implementations of Hirshfeld atom refinement or transferable aspherical atom models), unless the form factors are refinable parameters (for example multipole modelling). To evaluate this general approximation for one specific method, a numerical differentiation was implemented within the *NoSpherA2* framework to calculate the derivatives of the structure factors in a Hirshfeld atom refinement directly as accurately as possible, thus bypassing the approximation altogether. Comparing wR_2 factors and atomic parameters, along with their uncertainties from the approximate and numerically differentiating refinements, it turns out that the impact of this approximation on the final crystallographic model is indeed negligible.

1. Introduction

The quality of diffractometer equipment for X-ray crystallography has increased enormously over the last few decades: new detector technology, ever more intense radiation sources and enough computer power to handle large amounts of measurement frames all have led to more precise and accurate X-ray diffraction data than ever before. There is a wealth of chemical information in these improved diffraction data, and yet, these opportunities are largely ignored. X-ray diffraction data are still modelled in essentially the same way as they were 100 years ago. In obtaining the crystallographic model, spherical, non-interacting atomic electron densities are used – this is the so-called independent atom model (Compton, 1915).

It has been known for as long as the spherical model has existed that non-spherical contributions to atomic electron densities (caused by bonding in the molecular and crystal field) could potentially be observable from the X-ray diffraction pattern (Debye, 1915; Coppens, 1967). One can calculate these non-spherical atomic electron densities quantum-mechanically and then use them to generate crystallographic models, for example employing Hirshfeld atom refinement (HAR) (Jayatilaka & Dittrich, 2008; Capelli *et al.*, 2014). This is the approach we follow in this paper. In contrast, multipole

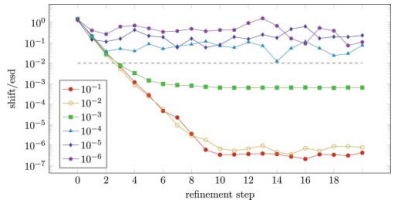

model refinements have been developed to introduce further parameters to refine the non-spherical atomic electron densities (Hansen & Coppens, 1978; Stewart, 1977; Koritsanszky & Coppens, 2001). Variations of this approach, such as databases based on the multipole model, so-called transferable aspherical atom models (TAAM), have also been pioneered (Bąk *et al.*, 2011; Jarzembska & Dominiak, 2012; Domagała *et al.*, 2012; Dittrich *et al.*, 2006; Jha *et al.*, 2020). All such non-spherical approaches are part of the field of quantum crystallography. For more details, we refer readers to overview articles (Grabowsky *et al.*, 2017; Genoni *et al.*, 2018; Macchi, 2020; Genoni & Macchi, 2020).

Using any of the mentioned quantum-crystallographic techniques will generate crystallographic models that are significantly more accurate in terms of atomic coordinates and displacement parameters, as well as agreement statistics, than anything obtainable from the spherical approach. This applies especially to hydrogen-atom parameters which are now much closer to those obtained by neutron diffraction (Woińska *et al.*, 2016; Fugel *et al.*, 2018; Sanjuan-Szklarz *et al.*, 2020; Jha *et al.*, 2020; Dittrich *et al.*, 2017; Wieduwilt *et al.*, 2021; Malaspina *et al.*, 2020).

We have recently introduced an entirely general way to handle non-spherical form factors in the refinement engine *olex2.refine* (Bourhis *et al.*, 2015). This has been followed by a new implementation of HAR in *Olex2* (Dolomanov *et al.*, 2009) called *NoSpherA2* (Non-Spherical Atoms in *Olex2*), which we believe will make sophisticated non-spherical refinement models generally accessible and very easy to use (Kleemiss *et al.*, 2021).

When employing non-spherical form factors, additional issues arise, such as the iterative update of form factors as the model changes (Capelli *et al.*, 2014), the use of finite-sized bases and the level of theory employed. There is also one fundamental approximation not addressed in the literature: when calculating the derivatives of the structure factors (as required for the least-squares refinement) the contributions of the derivatives of atomic form factors have thus far been neglected. It is important to make sure that this approximation is valid, especially since there is convincing evidence that the use of non-spherical form factors yields significantly improved structure models. In this study, the approximation is only tested and probed for the method HAR, but it is also relevant for other cases of non-spherical structure refinement such as other HAR variants (Malaspina *et al.*, 2019; Chodkiewicz *et al.*, 2020) or TAAM where the atomic form factors are not refinable parameters. It would not be relevant, though, for multipole modelling where the multipole populations, and consequently the form factors, are refinable parameters.

To explain this approximation, let us briefly discuss how the least-squares minimization process leads to this. The ultimate aim of the least-squares minimization is to modify the theoretical model in such a way that the theoretical results are in the best agreement with the observed data. Least-squares minimization needs the partial derivatives of the structure factors. The structure factors are dependent on the atomic form factors, which are the Fourier transforms of the electron-density functions of the atoms. In the current non-spherical refinement implementation in *olex2.refine*, the derivatives of the non-spherical form factors with respect to model parameters are chosen to be zero (that is, neglected) in the computation of these structure-factor derivatives. The method utilizing this approximation is henceforth called *approximate non-spherical refinement*. A fundamental question is whether this approximation of the derivatives has a noticeable impact on the refinement process. It is this question that is the motivation for this paper.

To answer this question, we implemented a non-spherical refinement process which uses as accurate as possible partial derivatives of the structure factors. Since these partial derivatives cannot be computed analytically and exactly, we use numerical differentiation. We refer to such refinement as *numerical non-spherical refinement*. The disadvantage of numerical non-spherical refinement is that it is too time-consuming for practical use (see Section 2.5). However, it is an ideal tool to test the impact of the approximation used in approximate non-spherical refinement. Details of these different refinement procedures are presented in Section 2.

Our investigations, based on crystals of the molecules ammonia, epoxide and L-alanine, begin with testing the robustness and validity of numerical non-spherical refinement – first determining appropriate step sizes to be used for the numerical differentiation, then confirming that its results are consistent, convergent and that the wR_2 factors are reduced (in comparison with approximate non-spherical refinement). This is carried out in Section 3.

We continue in Section 4 by comparing classical spherical refinement and approximate non-spherical refinement against numerical non-spherical refinement. Our comparison criteria comprise wR_2 factors, X—H distances and the positioning of the individual atoms in the unit cell under the different refinement processes. In addition, we investigate dependence of both approximate and numerical non-spherical refinement results on the quantum-mechanical basis sets.

In Section 5 we investigate the standard uncertainties of the least-squares minimization in the different refinement processes.

Expanded mathematical details regarding the least-squares minimization process and uncertainties are presented in Appendices *A* and *B*.

This article makes no statement about the best refinement method to provide the most accurate model of a real-world crystal. Instead, this paper is concerned with the numerical significance of a simplification used in the computation of the theoretical structure-factor derivatives. We believe this investigation is very important: if the approximation were found to have a significant impact on refinement results, this would require a rethink of the currently implemented method of non-spherical refinement.

2. The three main refinement procedures

The purpose of this section is to present the approximation under investigation and to discuss refinement procedures

which are at the centre of our investigations: classical *spherical refinement*, *approximate non-spherical refinement* and *numerical non-spherical refinement*.

Any crystallographic structure refinement depends on the provision of atomic form factors. Form factors are utilized in the computation of the structure factors which, in turn, enter into the derivation of the shift via a least-squares minimization method. The structure factor is computed from the form factors via the *crystallographic model formula*:

$$F_c(\mathbf{x},\mathbf{h}) = \sum_{j=1}^{N_{\text{atoms}}} f_j(\mathbf{z},\mathbf{h}) \underbrace{\exp(2\pi i \mathbf{h}^\top \mathbf{z}_j)\exp(-\mathbf{h}^\top \mathbf{U}_j \mathbf{h})}_{=G_j(\mathbf{x},\mathbf{h})}, \quad (1)$$

where N_{atoms} is the number of atoms in the unit cell, $\mathbf{z}_j$ is the position of the atom j and $\mathbf{U}_j$ is the matrix of its anisotropic displacement parameters (ADPs). Additionally, $f_j(\mathbf{z},\mathbf{h})$ is the form factor of the atom j translated to the origin. This form factor, in the non-spherical case, is dependent on the atomic positions $\mathbf{z}$ (comprised of the individual atomic positions $\mathbf{z}_j$) and the reciprocal-lattice vector $\mathbf{h}$. The $\mathbf{z}_j$ and $\mathbf{U}_j$ values form the vector $\mathbf{x}$ of refined parameters describing the model, taking into account the symmetry restrictions where necessary. For example, if all atoms of the molecule are in general positions, we have three positional parameters and six ADPs for each atom which, in succession, form the vector $\mathbf{x}$. The jth atom A in the model vector $\mathbf{x} \in \mathbb{R}^{9N_{\text{atoms}}}$ is then represented by the 9-tuple $(x_A, y_A, z_A, U^A_{11}, U^A_{22}, U^A_{33}, U^A_{12}, U^A_{13}, U^A_{23})$, with $\mathbf{z}_j = (x_A, y_A, z_A)$ and

$$\mathbf{U}_j = \begin{bmatrix} U^A_{11} & U^A_{12} & U^A_{13} \\ U^A_{21} & U^A_{22} & U^A_{23} \\ U^A_{31} & U^A_{32} & U^A_{33} \end{bmatrix},$$

where $U^A_{21} = U^A_{12}$, $U^A_{31} = U^A_{13}$ and $U^A_{32} = U^A_{23}$.

The least-squares minimization process requires the derivatives of the structure factors, given by

$$\frac{\partial F_c}{\partial x_n}(\mathbf{x},\mathbf{h}) = \sum_{j=1}^{N_{\text{atoms}}} \underbrace{\frac{\partial f_j}{\partial x_n}(\mathbf{z},\mathbf{h}) G_j(\mathbf{x},\mathbf{h})}_{(*)} + f_j(\mathbf{x},\mathbf{h}) \frac{\partial G_j}{\partial x_n}(\mathbf{x},\mathbf{h}). \quad (2)$$

The motivation of this paper is to investigate the consequences of the common setting of $(*) = 0$ which, whilst true for spherical refinement (described below), is no longer true for non-spherical refinements. It is worth clarifying that the coordinates x_n of $\mathbf{x}$ are related to either the positional ($\mathbf{z}_j$) or ADP ($\mathbf{U}_j$) components. We note that for x_n related to ADPs, the derivative $(\partial f_j/\partial x_n)(\mathbf{z},\mathbf{h})$ is always zero (as f_j has no dependence on the ADPs), and thus for those parameters we can in fact determine the derivatives $\partial F_c/\partial x_n$ analytically (since the functions G_j are simple exponentials with explicitly given derivatives).

Further details with regards to the least-squares minimization process, including a useful description of a modified design matrix $\tilde{D}$ as well as distinguishing where structure-factor derivatives are required, are shown in Appendix *A*.

2.1. Classical spherical refinement and multipole modelling

Spherical refinement is based on the independent atom model (IAM), which provides spherically symmetric functions for the form factors. These form factors are not only spherically symmetric, but also depend only on the atom type and charge – that is, they do not change with the model of the crystal. This leads to the simple deduction that any change to the model will not result in a change to the form factor – that is, the derivative $\partial f_j/\partial x_n$ is always zero, and thus the term $(*)$ in (2) is zero. In the case of multipolar atom refinement, the derivative of the non-spherical atom form factors is analytically solvable since the density is a function of the spherical harmonic occupancy and radial kappa values and the atomic parameters in the vector $\mathbf{x}_j$; therefore the approximation scrutinized here does not apply.

2.2. Approximate non-spherical refinement

It is natural to assume that choosing physically more accurate form factors and more accurate values of their derivatives for the specific model consequentially will lead to more accurate results from the least-squares minimization process. To obtain these physically more meaningful form factors, we utilize quantum-mechanical computations to determine the electron-density function ρ^{mol} of the whole molecule. Then, this function is partitioned into individual atoms utilizing a weight function

$$w_j(\mathbf{r}) = \frac{\rho_j^{\text{sph}}(\mathbf{r})}{\rho^{\text{pro}}(\mathbf{r})},$$

(Hirshfeld, 1977) where $\mathbf{r}$ is a point in space, ρ_j^{sph} is the spherical atomic density associated to the jth atom, and $\rho^{\text{pro}}(\mathbf{r}) = \sum_j \rho_j^{\text{sph}}(\mathbf{r})$ is the promolecule density generated from the spherical atomic densities. Given a molecular electron density ρ^{mol}, we then assign each atom its non-spherical electron-density function

$$\rho_i^{\text{nonspher}}(\mathbf{r}) = w_j(\mathbf{r})\rho^{\text{mol}}(\mathbf{r}).$$

This is commonly known as Hirshfeld partitioning or Hirshfeld stockholder partitioning and is used in HAR (Jayatilaka & Dittrich, 2008). These atomic non-spherical electron-density functions are transformed into non-spherical form factors f_j via a Fourier transform. Fortunately, this formalism introduces no additional refinement parameters and thus cannot lead to overfitting.

With current technologies, however, we are not aware of any practically feasible method to compute the derivatives $\partial f_j/\partial x_n$ of these non-spherical form factors analytically for HAR. There might be ways to do it in the case of multipole database approaches if one morphs the form factors based on slight changes in positioning of the atoms within a fragment, but this is not the topic of this paper. Because of this, in the currently implemented non-spherical refinement in *olex2.refine* using *NoSpherA2*, we make an approximation – that the form factor derivatives $\partial f_j/\partial x_n$ are close enough to zero to be taken as zero (Kleemiss *et al.*, 2021). Therefore, we set the term $(*)$ in (2) to zero. This leads to a process which we

call *approximate non-spherical refinement*. In short, we use molecular quantum-mechanical computations and partitioning to obtain better form factors, but we use the simplest approximation of their derivatives by setting them equal to zero. Approximate non-spherical refinement is illustrated in the flowchart in Fig. 1.

Approximate non-spherical refinement begins with an initial model obtained through classical spherical refinement. Then, by passing this model to a quantum-mechanical calculation program, a wavefunction is calculated and transferred to the *NoSpherA2* software in the form of a wfn or wfx file. *NoSpherA2* converts this into an electron-density function for the model, partitions it, and computes the non-spherical form factors, which are returned in a .tsc file for further use (Kleemiss *et al.*, 2021; Midgley *et al.*, 2019).

We then utilize least-squares minimization, bringing in other information such as the observed intensities I_o and weights, calculating F_c and approximating $\partial F_c/\partial x_n$ by the analytical expression (2) [with $(*) = 0$] and using these to calculate a shift to the model which should result in a better agreement with observed data.

We run this loop repeatedly as in a classical refinement, until the model is converged (by the standard shift/e.s.d. ≤ 0.01 rule, where 'e.s.d.' is the estimated standard deviation, also referred to as standard uncertainty, of the model parameter), or we have reached a limit n_{max} of how many times we are comfortable doing a refinement cycle without recalculating the .tsc file, as this will become increasingly outdated with increasing changes to the model. As calculation of the .tsc file is time consuming, we prefer to get more 'use' out of the same file before the model changes too significantly.

We then compare this output model to the input model – if they are *sufficiently close* (for example, if the maximal parameter difference/e.s.d. ≤ 0.01), then the refinement has converged and we take the output model as our final model. Here we also limit the number of iterations to m_{max} and we terminate the procedure if this convergence criterion has not been satisfied.

2.3. Numerical non-spherical refinement

The third refinement method uses the same quantum-mechanically calculated non-spherical form factors given via a .tsc file. However, a numerical procedure to derive improved values of the derivatives $\partial F_c/\partial x_n$ (in coordinates x_n representing positional parameters) is included, without the simplification that $(*)$ is zero. Since differentiation describes the change of F_c in the direction of x_n, we use models which are close neighbours of the current model **x**. We alter a single positional parameter x_n by a small amount to calculate the derivative $\partial F_c/\partial x_n$. This allows us to perform a mathematically more accurate least-squares minimization process. We refer to this process in this paper as *numerical non-spherical refinement*. As in the case of approximate non-spherical refinement, no additional refinement parameters are introduced and thus we again avoid overfitting.

In the case of numerical non-spherical refinement, illustrated by the flowchart in Fig. 2, the initial model can be

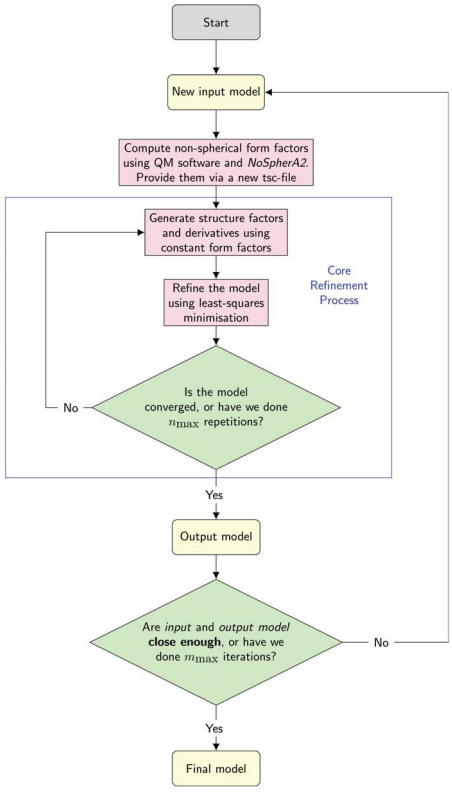

Figure 1
Flowchart illustration of approximate non-spherical refinement.

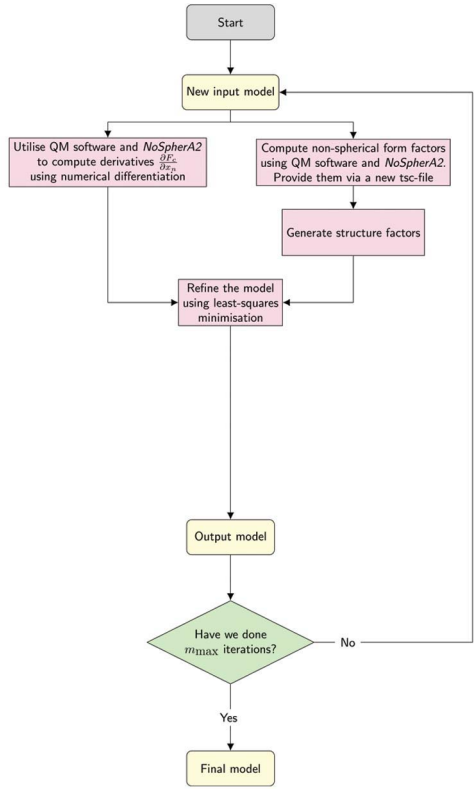

Figure 2
Flowchart illustration of numerical non-spherical refinement.

Table 1
Median time costs for one step of each non-spherical refinement process (in seconds).

Molecule	Approximate	Hybrid	Numerical
Ammonia	9.3	63	79
Epoxide	11.8	302	503
L-Alanine	47.2	2137	3783

either obtained by spherical refinement or by approximate non-spherical refinement. We utilize *NoSpherA2* in each iteration not only once for the computation of the form factors f_j of the given model but also multiple times for the calculation of the derivatives $\partial F_c/\partial x_n$ of the structure factor. In fact, each such partial derivative computation via numerical differentiation requires two additional quantum-mechanical and *NoSpherA2* computations and the time complexity of this process grows linearly with the number of atoms in the model. We additionally are cautious and reduce the risk of outdated quantum-mechanical data by only ever performing one refinement cycle with a given .tsc file. Additionally, we always carry out a full 20 steps whether or not the model has converged, to provide additional information as to whether a model remains in this status or whether it may still fluctuate. We record the model at each step and return the model with the lowest wR_2 factor as our final model. These settings are currently only used for test purposes, not as defaults in *NoSpherA2* for general use.

Typically, there are up to three derivative calculations per atom, corresponding to its x, y and z coordinates. These can sometimes be reduced by the symmetry of the molecule, as in the case of ammonia. As the ADPs have no part in the wavefunction calculation, and no impact on the form factors, all derivatives related to them are simply taken as in the approximate non-spherical case.

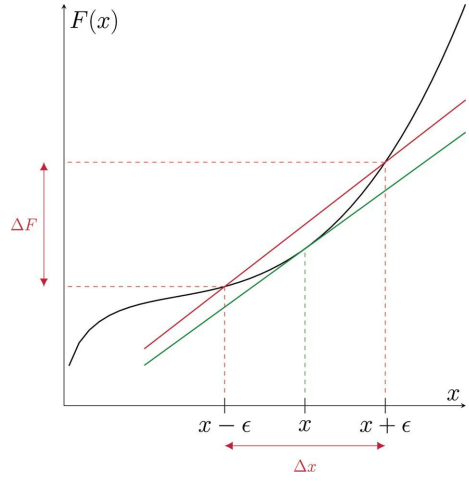

Figure 3
The principle behind numerical differentiation; the analytical derivative (slope of tangent) is shown in green whilst the numerical derivative (slope of secant) is shown in purple.

2.4. Hybrid refinement

Later in this article, we will also consider a 'hybrid' version between numerical and approximate non-spherical refinement, where only the derivatives related to the hydrogen atoms are computed more accurately via numerical differentiation, and all other derivatives are computed in the same way as in approximate non-spherical refinement. We introduce this compromise since each atom adds a lot of computational cost and hydrogen atoms typically show the biggest differences between numerical and approximate refinement. This allows a reduction in time cost whilst still largely retaining the benefit of numerical non-spherical refinement. This is referred to as *hybrid non-spherical refinement.*

2.5. Time cost

Time-cost comparisons of approximate, numerical and hybrid non-spherical refinements are presented in Table 1. We present the median time cost for one refinement step (that is, the generation and application of one shift vector) amongst 20 random refinement steps in each of the three refinement processes. These were carried out on a computer running Windows 10 utilizing 15 GB of RAM and three CPU cores.

As numerical non-spherical refinement requires a quantum-mechanical calculation twice for each positional parameter in $\mathbf{x}$, as well as one for the central F_{calc}, we expect it to take $(2 \times \#_{parameters} + 1)$ times as long to run as approximate non-spherical refinement does, which is reflected in this table. This is a theoretical time requirement, not an implementation one, so it gets less and less viable for larger molecules, but is otherwise dependent on the speed of the method used. In the case of hybrid non-spherical refinement, we count only those positional parameters relating to hydrogen atoms. For example, in the case of L-alanine, one expects that numerical will take 79 times as long, and hybrid 43 times as long, as approximate non-spherical refinement.

2.6. Numerical differentiation

Let us finally provide a brief explanation of the method of *numerical differentiation* which we use for the computation of the partial derivatives $\partial F_c/\partial x_n$ in the case of numerical non-spherical refinement. For simplicity, the illustration in Fig. 3 presents the one-dimensional case.

As demonstrated in Fig. 3, the derivative is computed numerically as follows:

$$F'(x) \simeq \frac{\Delta F}{\Delta x} = \frac{F(x+\epsilon) - F(x-\epsilon)}{2\epsilon}. \qquad (3)$$

That is, the expression on the right-hand side of this equation is the slope of the purple line (where the slope of the green line is the actual derivative). Theoretically, the expression on the right-hand side of (3) is more and more accurate as the ϵ value becomes smaller. On the other hand, too small ϵ values lead numerically to increasingly significant rounding errors. The right choice of the step size $\epsilon > 0$ is therefore a compromise between these two inaccuracies.

In our many-dimensional case where the function is the structure factor F_c, we use the following expression:

$$\frac{\partial F_c}{\partial x_n}(\mathbf{x},\mathbf{h}) \simeq \frac{F_c(\mathbf{x}+\epsilon\mathbf{e_n},\mathbf{h}) - F_c(\mathbf{x}-\epsilon\mathbf{e_n},\mathbf{h})}{2\epsilon},$$

where $\mathbf{e_n}$ is the nth standard basis vector associated to the parameter x_n. The next section (Section 3) of this paper is concerned with a good choice of the step size $\epsilon > 0$ in numerical non-spherical refinement and with robustness investigations of the numerical differentiation used in this process.

We consider the numerical non-spherical refinement procedure as the most mathematically accurate at our disposal. Therefore, in Sections 4 and 5 of this paper we compare its performance with approximate non-spherical refinement which is currently used in *NoSpherA2* interfaced to *olex2.refine*, and spherical refinement as routinely used in *olex2.refine*.

2.7. Experimental settings

In this work, we used the following settings. The non-spherical refinement method HAR was performed utilizing *Olex2-1.5* (Dolomanov *et al.*, 2009), *NoSpherA2* and *ORCA* (Neese, 2012, 2018). The basis set chosen was def2-TZVPP with the method PBE and high integration accuracy, unless mentioned otherwise. Refinement was done using standard unit weights, using the Gauss–Newton minimization method. The Cartesian step size for numerical non-spherical refinements was $\delta = 10^{-3}$ Å if not otherwise specified. The code used to perform numerical refinements can be found in the supporting information.

3. The quality of numerical non-spherical refinement

This section is concerned with the quality of numerical non-spherical refinement. In particular, we test it with regards to the following criteria:

(i) wR_2 reduction. Numerical non-spherical refinement should result in a smaller wR_2 factor than spherical or approximate non-spherical refinement.

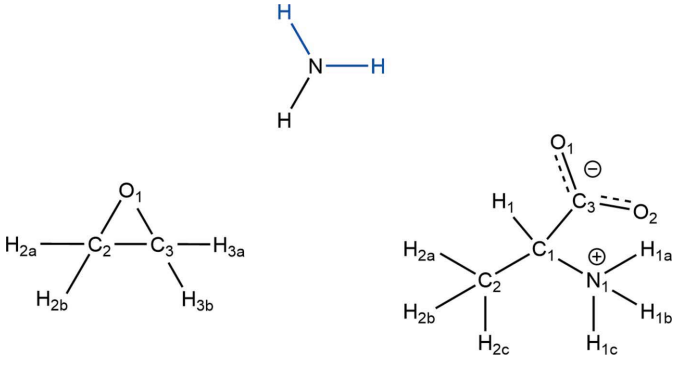

Figure 4
The chemical structures and atom labels of ammonia (top), epoxide (left) and L-alanine (right). Because of crystallographic symmetries in ammonia, two symmetry-equivalent H atoms are shown in blue.

(ii) Convergence. When numerical non-spherical refinement has reached a wR_2 minimum, the model should no longer fluctuate – future shift vectors should be sufficiently small.

(iii) Consistency. The minimum should be independent of the start model used for the numerical non-spherical refinement.

Note that the model and the partial derivatives are given in fractional coordinates with respect to the unit cell. The computation of partial derivatives in positional directions via numerical differentiation uses a certain step size ϵ in fractional coordinates which translates into a corresponding Cartesian step size δ in Cartesian coordinates. In order to find the most suitable choice of Cartesian step size δ, we investigate and compare results for numerical differentiation with δ choices from 10^{-1} to 10^{-6} Å.

In our tests, we employ data sets collected from crystals of three different molecules – ammonia (NH_3) (Boese *et al.*, 1997), epoxide (C_2H_4O) (Grabowsky *et al.*, 2010) and L-alanine ($C_3H_7NO_2$) (Destro *et al.*, 1988; Grabowsky *et al.*, 2008) (see Fig. 4 for their chemical structures, see Table S1 in the supporting information for further details). In the latter two molecules, all atoms are in general positions and the vector $\mathbf{x}$ describing the model has nine parameters for each atom (three positional parameters and six ADPs). The space group of NH_3 is $P2_13$ and its model is determined by nine parameters for the H atom, and only three parameters for the N atom as it is restricted to the symmetry $x = y = z$ (meaning also that $U_{11} = U_{22} = U_{33}$ and $U_{12} = U_{13} = U_{23}$). Of course, in the presence of symmetries, the vector $\mathbf{x}$ can be expanded to a larger vector $\mathbf{y} = \mathbf{y}(\mathbf{x})$ which provides all nine parameters for each atom in the molecule.

The least-squares process is focused on minimizing the wR_2 factor. The wR_2 factor is defined as

$$wR_2(\mathbf{x}) = \left\{\frac{\sum_{\mathbf{h}} w(\mathbf{h})[Y_o(\mathbf{h}) - \tilde{K}(\mathbf{x})Y_c(\mathbf{x},\mathbf{h})]^2}{\sum_{\mathbf{h}} w(\mathbf{h})Y_o(\mathbf{h})^2}\right\}^{1/2}. \quad (4)$$

Here, $Y_o(\mathbf{h})$ are the observed intensities, $Y_c(\mathbf{x},\mathbf{h})$ the calculated intensities (depending on the model $\mathbf{x}$), and $w(\mathbf{h})$ the weight associated to the Miller triple $\mathbf{h}$. Here we also have the scaling factor $\tilde{K}(\mathbf{x})$, an analytically calculated constant multiplier across all Y_c which scales Y_c to minimize the weighted norm (6) of the difference vector $Y_o(\mathbf{h}) - \tilde{K}(\mathbf{x})Y_c(\mathbf{x},\mathbf{h})$.

The wR_2 factor can also be written as a quotient of *weighted norms*

$$wR_2(\mathbf{x}) = \frac{\|\tilde{r}(\mathbf{x})\|_w}{\|Y_o\|_w} \quad (5)$$

of the residual vector $\tilde{r}(\mathbf{x}) = Y_o(\mathbf{h}) - \tilde{K}(\mathbf{x})Y_c(\mathbf{x},\mathbf{h})$ and the observed intensities Y_o.

Here, the weighted norm of a vector $\mathbf{v}$ is given by

$$||\mathbf{v}||_w = \left\{\sum_h [w(\mathbf{h})v(\mathbf{h})^2]\right\}^{1/2}. \quad (6)$$

That is, $wR_2(\mathbf{x})$ is the difference between the model and observed intensities relative to the strength of the observed intensities – it provides a *percentage disagreement*.

Henceforth, we will use the following notation: $\mathbf{x}_{\text{spher}}$ denotes the final model obtained via spherical refinement and, similarly, $\mathbf{x}_{\text{appr}}$ and $\mathbf{x}_{\text{num}}$ denote the corresponding final models for the non-spherical refinements. Starting with an initial model $\mathbf{x}_0 = \mathbf{x}_{\text{spher}}$ or $\mathbf{x}_0 = \mathbf{x}_{\text{appr}}$, numerical non-spherical refinement iteratively generates a sequence $\mathbf{x}_j$ of 20 models via $\mathbf{x}_{j+1} = \mathbf{x}_j + \mathbf{s}_j$, where $\mathbf{s}_j$ is the jth shift vector (see Appendix *A* for more details). Then $\mathbf{x}_{\text{num}}$ is the model $\mathbf{x}_j$ with the minimal wR_2 factor within this sequence.

The maximal shift/e.s.d. for ammonia over 20 refinement steps for each choice of $\delta \in \{10^{-1}, 10^{-2}, 10^{-3}, 10^{-4}, 10^{-5}, 10^{-6}$ Å$\}$ is shown in Fig. 5. The 20 refinement steps are represented by the horizontal axis. At step j, each parameter in the shift vector $\mathbf{s}_j$ is divided by the corresponding uncertainty of the model $\mathbf{x}_j$ and the maximum over these quotients is taken. This value shift/e.s.d. is represented vertically above each step.

If shift/e.s.d. is lower than 0.01 the model is considered settled as the shifts cannot cause a significant change to the parameters (compared with their uncertainties). Fig. 5 shows that this convergence threshold (represented by the dashed line) is not reached for $\delta \in \{10^{-4}, 10^{-5}, 10^{-6}$ Å$\}$. Similar diagrams for epoxide and L-alanine are presented in the supporting information, and also include the line for hybrid non-spherical refinement at $\delta = 10^{-3}$ Å (Figs S2–S4). For $\delta \in \{10^{-1}, 10^{-2}, 10^{-3}$ Å$\}$, convergence is reached from the third step onwards. For such choices of δ, the criterion of convergence is achieved.

Fig. 6 shows the wR_2 factors of numerical non-spherical refinement for ammonia. Figures for epoxide and L-alanine can be found in the supporting information (Figs. S12 and S19, respectively), alongside diagrams presenting the finer details for all three molecules (Figs. S6–S22). We note that many of the points (in Fig. 6) overlap, and all journeys have the same start point of 1.944%. In particular, $\delta = 10^{-1}$ Å, …, 10^{-4} Å have very similar essentially horizontal wR_2 progressions. Since the wR_2 factor decreases compared with the start value, numerical non-spherical refinement provides wR_2 reduction (compared with approximate non-spherical refinement). Fig. 6 also indicates that $\delta = 10^{-5}$ Å and 10^{-6} Å provide results with larger wR_2 factor shifts later in the journey (outliers). We therefore consider these δ values as less suitable for a systematic investigation, since they lead to computational instabilities in the numerical procedure. Such increased errors at low δ are typically related to errors in the storage of numbers. In our case, this could be related to the way that *NoSpherA2* passes information, such as atomic positions, to the quantum-mechanical program, and more precise passing of information could allow smaller δ choices. Presently, we are limited by the 8-digit precision of the wfn file, which can lead to an error of up to 2×10^{-8} Å in the input to the quantum-mechanical program (this is many orders of magnitude smaller than experimental error).

In view of the above results and in consideration with the results from the other molecules, we decided to fix the Cartesian step size to be $\delta = 10^{-3}$ Å for all numerical differentiations in the remainder of this paper. This usually gives lower wR_2 factors whilst satisfying convergence. This can be seen in Figs. S2–S4, S13 and S20 in the supporting information.

To provide evidence of the general applicability of our verification tool for the assumption, we utilized a different generation scheme (TAAM) in the supporting information, with figures akin to Figs. 5 and 6 shown in Figs. S26–S28 (Kumar *et al.*, 2019; Chodkiewicz *et al.*, 2018; Gildea *et al.*, 2011).

After numerical refinement, employing approximate refinement steps will rapidly return to the approximate minimum with a slightly higher wR_2. In Fig. 7, we ran five steps of approximate refinement followed by five steps of numerical refinement on ammonia, and repeated (we began at the spherical minimum, so the first two very large steps have been cut off. This graph for the other molecules and the full motion from $\mathbf{x}_{\text{spher}}$ can be found in Figs. S9–S11, S16–S18 and S23–S25 in the supporting information). It is clear to see that each

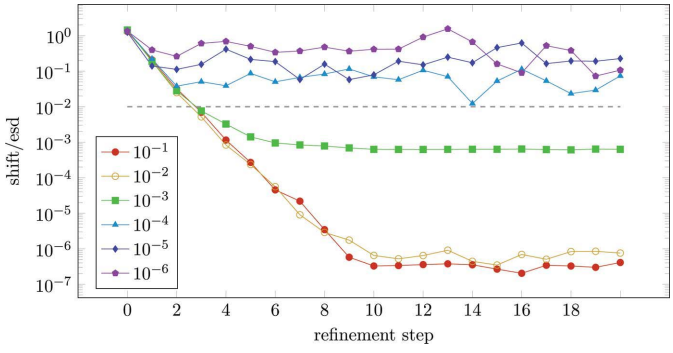

Figure 5
Maximal shift/e.s.d. for numerical non-spherical refinement starting from $\mathbf{x}_{\text{appr}}$ for $\delta = 10^{-1}$ Å, …, 10^{-6} Å (ammonia).

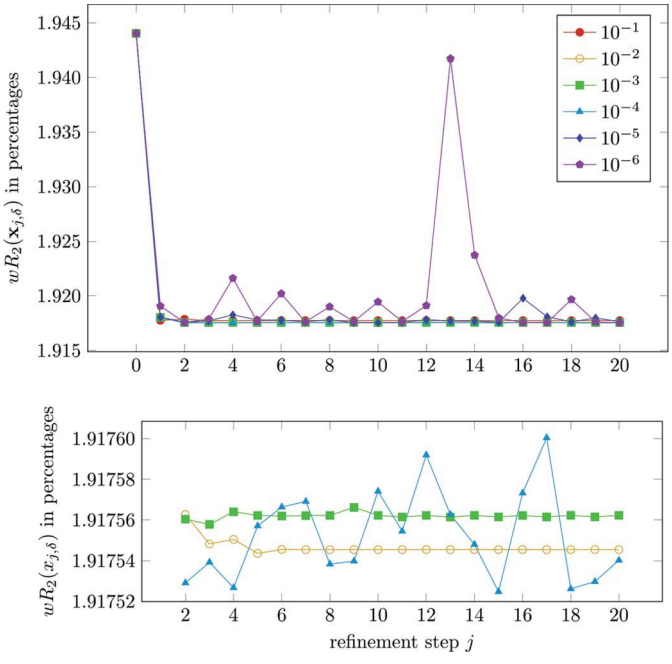

Figure 6
The progression of $wR_2(\mathbf{x}_j)$ for $j = 0, 1, \ldots, 20$ and for $\delta = 10^{-1}, \ldots, 10^{-6}$ Å starting from $\mathbf{x}_{\text{appr}}$ (ammonia).

refinement method returns to its own minimum within only a few steps, and that these are distinct. This means that approximate and numerical refinements converge to slightly different minima although both methods aim to minimize the same target function (measured by wR_2) and both seem to converge to their respective minima equally rapidly. Using the wrong atom form factor derivatives (namely assuming them to be zero) leads consistently to a small deviation from the numerical refinement result of the approximate refinement process into a less optimal minimum. This provides further evidence that numerical refinement provides wR_2 reduction and is also a first indication for its consistency.

Finally, we compare the journeys of numerical non-spherical refinement beginning at the two different start models $\mathbf{x}_{\text{spher}}$ and $\mathbf{x}_{\text{appr}}$, as shown in Table 2.

The first four columns of Table 2 demonstrate the typical convergence measures shift/e.s.d. and wR_2 factor for numerical non-spherical refinement processes starting from $\mathbf{x}_{\text{spher}}$ and from $\mathbf{x}_{\text{appr}}$. Italic values in the first two columns mean that the convergence criterion 'shift/e.s.d. <0.01' is achieved while bold values mean that it is not. As expected, the initial wR_2 factor of numerical non-spherical refinement starting from $\mathbf{x}_{\text{spher}}$ is much higher than the initial wR_2 factor of numerical non-spherical refinement starting from $\mathbf{x}_{\text{appr}}$, but the wR_2 factors of both journeys agree already after a few steps in both refinement processes. Note that all wR_2 factors are computed using non-spherical form factors.

In the last column of Table 2 we present the difference d (in 10^{-6} Å) between corresponding atom sites of the two models obtained via k numerical non-spherical refinement steps starting from $\mathbf{x}_{\text{spher}}$ and $\mathbf{x}_{\text{appr}}$, respectively. For example, the third entry 2458×10^{-6} Å is the difference between the atom site of H of ammonia after three numerical non-spherical refinement steps starting from $\mathbf{x}_{\text{spher}}$ and the same atom site of H after three numerical non-spherical refinement steps starting from $\mathbf{x}_{\text{appr}}$ (since this distance is maximal for H amongst all corresponding atoms). Our investigations confirm that this maximum is always attained by one of the H atoms (see Table S2 in the supporting information). These maximal differences between sites of corresponding atoms shrink significantly after each refinement step until they reach values around 10^{-5} Å. Since, after about seven refinement steps, these distances are about the same size as the maximal Cartesian shifts of the individual atoms from the model $\mathbf{x}_k$ to the model $\mathbf{x}_{k+1}$ (these maximal shifts can be found in Table S2 of the supporting information), we can safely conclude that convergence of both refinement processes is essentially obtained after at most seven refinement steps. Moreover, since the two refinement processes from different start models $\mathbf{x}_{\text{spher}}$ and $\mathbf{x}_{\text{appr}}$ lead after about seven refinement steps to models whose atom sites agree up to 10^{-5} Å, the table proves in particular consistency of numerical non-spherical refinement.

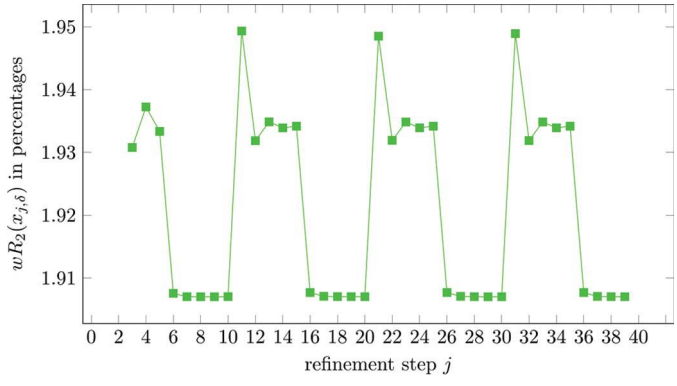

Figure 7
The progression of $wR_2(\mathbf{x}_j)$ for $j = 3, 4, \ldots, 40$ and for $\delta = 10^{-3}$ Å, alternating between five steps of approximate and five steps of numerical refinement (ammonia).

Table 2
Progression of refinement values from $\mathbf{x}_{\text{spher}}$ and $\mathbf{x}_{\text{appr}}$ via numerical non-spherical refinement with $\delta = 10^{-3}$ Å.

In the first two columns, if the shift/e.s.d. is below 0.01, it is shown in italic, else bold. The final column represents the maximal difference d between sites of corresponding atoms through numerical non-spherical refinement from these two start points.

Step	Shift/e.s.d. ($\times 10^5$) (from $\mathbf{x}_{\text{spher}}$)	Shift/e.s.d. ($\times 10^5$) (from $\mathbf{x}_{\text{appr}}$)	wR_2 (from $\mathbf{x}_{\text{spher}}$)	wR_2 (from $\mathbf{x}_{\text{appr}}$)	d (in 10^{-6} Å)
Ammonia					
$k = 0$	**392693**	**143955**	9.2821%	1.9440%	126974
$k = 1$	**198189**	**18797**	2.6092%	1.9180%	20665
$k = 2$	**47387**	**2818**	1.9216%	1.9176%	2458
$k = 3$	**7724**	*760*	1.9176%	1.9176%	380
$k = 4$	**1823**	*324*	1.9175%	1.9176%	102
$k = 5$	*592*	*142*	1.9176%	1.9176%	36
$k = 6$	*140*	*78*	1.9176%	1.9176%	11
$k = 7 \ldots 20$	*≤88*	*≤119*	1.9176%	1.9176%	≤5
Epoxide					
$k = 0$	**674626**	**51117**	12.0375%	4.6551%	130527
$k = 1$	**281762**	**4568**	4.9113%	4.6536%	21095
$k = 2$	**35810**	*812*	4.6561%	4.6536%	3093
$k = 3$	**6868**	*476*	4.6537%	4.6536%	461
$k = 4$	**1365**	*152*	4.6536%	4.6536%	136
$k = 5$	*292*	*88*	4.6536%	4.6536%	38
$k = 6$	*138*	*102*	4.6536%	4.6536%	16
$k = 7 \ldots 20$	*≤99*	*≤126*	4.6536%	4.6536%	≤11
L-Alanine					
$k = 0$	**992154**	**50245**	6.4989%	3.2299%	126479
$k = 1$	**308603**	**3568**	3.3127%	3.2291%	24140
$k = 2$	**32231**	*641*	3.2298%	3.2291%	1818
$k = 3$	**7711**	*244*	3.2291%	3.2291%	237
$k = 4$	**1838**	*176*	3.2291%	3.2291%	59
$k = 5$	*431*	*202*	3.2291%	3.2291%	20
$k = 6$	*214*	*194*	3.2291%	3.2291%	16
$k = 7 \ldots 20$	*≤190*	*≤267*	3.2291%	3.2291%	≤14

4. Comparison of refinement minima

This section is concerned with a direct comparison of the final models obtained via our different refinement methods. Within this, we work with the assumption that numerical non-spherical refinement is the best theoretical refinement method for our X-ray diffraction data, and measure the quality of the results obtained with spherical refinement, approximate non-spherical refinement and hybrid non-spherical refinement against those obtained from numerical refinement. Recall that all refinements from now on are based on the Cartesian step size $\delta = 10^{-3}$ Å.

Table 3
wR_2 factors and interatomic distances from different refinement techniques for three X-ray data sets, and reference neutron data for L-alanine.

	$\mathbf{x}_{\text{spher}}$ †	$\mathbf{x}_{\text{appr}}$	$\mathbf{x}_{\text{hybr}}$	$\mathbf{x}_{\text{num}}$	$\mathbf{x}_{\text{neutron}}$ ‡
Ammonia					
wR_2	2.39%	1.944%	1.918%	1.918%	
N—H	0.855 (6)	0.973 (5)	0.979 (5)	0.979 (5)	
Epoxide					
wR_2	6.71%	4.655%	4.654%	4.654%	
H2*a*—C2	0.995 (8)	1.095 (7)	1.095 (6)	1.095 (6)	
H2*b*—C2	0.975 (8)	1.079 (6)	1.080 (5)	1.080 (5)	
H3*a*—C3	0.975 (11)	1.102 (8)	1.106 (7)	1.106 (7)	
H3*b*—C3	0.968 (10)	1.090 (7)	1.090 (7)	1.090 (7)	
C2—O1	1.4367 (8)	1.4316 (5)	1.4316 (5)	1.4316 (5)	
C3—O1	1.4425 (7)	1.4359 (5)	1.4359 (5)	1.4359 (5)	
C3—C2	1.4561 (9)	1.4577 (6)	1.4578 (6)	1.4578 (6)	
L-Alanine					
wR_2	6.04%	3.230%	3.229%	3.229%	
H1*a*—N1	0.923 (13)	1.006 (6)	1.007 (6)	1.007 (6)	1.0351 (16)
H1*b*—N1	0.936 (12)	1.019 (6)	1.019 (6)	1.019 (6)	1.0439 (16)
H1*c*—N1	1.085 (17)	1.045 (8)	1.050 (6)	1.050 (6)	1.0534 (15)
H1—C1	1.002 (9)	1.090 (5)	1.091 (4)	1.091 (4)	1.0993 (15)
H2*a*—C2	0.993 (13)	1.100 (7)	1.101 (6)	1.101 (6)	1.0919 (19)
H2*b*—C2	0.978 (11)	1.094 (7)	1.095 (6)	1.095 (6)	1.0945 (18)
H2*c*—C2	1.005 (10)	1.089 (6)	1.090 (5)	1.090 (5)	1.095 (2)
C1—N1	1.4919 (7)	1.4905 (4)	1.4906 (4)	1.4906 (4)	1.4891 (7)
C2—C1	1.5260 (7)	1.5264 (4)	1.5264 (4)	1.5264 (4)	1.5266 (8)
C3—C1	1.5329 (8)	1.5344 (4)	1.5344 (4)	1.5344 (4)	1.5360 (7)
O1—C3	1.2493 (6)	1.2478 (3)	1.2478 (3)	1.2478 (3)	1.2479 (9)
O2—C3	1.2668 (7)	1.2664 (3)	1.2664 (3)	1.2664 (3)	1.2661 (8)

† wR_2 factors for $\mathbf{x}_{\text{spher}}$ are calculated using spherical form factors. ‡ Neutron data are taken from Malaspina *et al.* (2019) and are only presented for L-alanine as there are no neutron data for ammonia and epoxide to our knowledge. No wR_2 value given, since the wR_2 value in Laue neutron and single-wavelength X-ray refinement statistics is not directly comparable.

Whilst in the previous section we focused on the wR_2 factor, we will now be comparing more specific values such as the model parameters themselves and the interatomic distances. The results of this section focus on the exact computational results. Considerations of statistical uncertainties will be investigated in the next section.

In this section, hybrid non-spherical refinement is also analysed. Hybrid non-spherical refinement takes numerical non-spherical derivatives for the H atoms, but takes approximate non-spherical derivatives for any other atoms (see Appendix *A* for further details). This allows a reduction in time cost (roughly corresponding to the proportion of H atoms in the molecule – see Section 2.5) compared with numerical, whilst still conveying many of the benefits of full numerical non-spherical refinement. In keeping with previous notation, the final model of hybrid non-spherical refinement (which is again chosen to be the model with smallest wR_2 factor through the 20 refinement steps) is denoted $\mathbf{x}_{\text{hybr}}$.

4.1. wR_2 factors and interatomic distances

In Table 3 we present the wR_2 factor and interatomic distances of the models. We note that the wR_2 factor calculated at $\mathbf{x}_{\text{spher}}$ uses spherical form factors (accounting for the difference compared with those in Table 2, which are based on non-spherical form factors throughout).

One can clearly see the dramatic difference between $\mathbf{x}_{\text{spher}}$ and $\mathbf{x}_{\text{appr}}$ with regards to a drop in the wR_2 factor and increase of the interatomic distances. The difference from $\mathbf{x}_{\text{appr}}$ to $\mathbf{x}_{\text{hybr}}$ is much smaller, and the difference to $\mathbf{x}_{\text{num}}$ from $\mathbf{x}_{\text{hybr}}$ is almost non-existent. While the aim of this paper is to compare the refinement methods, for general interest, Table 3 also presents the corresponding distances for L-alanine obtained by neutron diffraction taken from Malaspina *et al.* (2019). The X—H distances from neutron diffraction are, as expected, in much better agreement with $\mathbf{x}_{\text{appr}}$, $\mathbf{x}_{\text{hybr}}$ and $\mathbf{x}_{\text{num}}$ than they are with $\mathbf{x}_{\text{spher}}$. Nevertheless, they are in most cases still longer than any of the X-ray-derived values in the non-spherical methods ($\mathbf{x}_{\text{appr}}$, $\mathbf{x}_{\text{hybr}}$ and $\mathbf{x}_{\text{num}}$), which may be related to the weak scattering signal of H atoms in X-ray diffraction [also see Capelli *et al.* (2014), Dittrich *et al.* (2017) for further discussion].

Table 4
Differences between the sites of atoms of $\mathbf{x}_{\text{num}}$ versus other models (in 10^{-7} Å).

The first column shows the difference between final models of numerical non-spherical refinement processes obtained from different start models $\mathbf{x}_{\text{spher}}$ and $\mathbf{x}_{\text{appr}}$, with the subscript 's' indicating that from $\mathbf{x}_{\text{spher}}$.

	$\|\mathbf{z}^{\text{C}}_{\text{num}} - \mathbf{z}^{\text{C}}_{\text{num,s}}\|$	$\|\mathbf{z}^{\text{C}}_{\text{num}} - \mathbf{z}^{\text{C}}_{\text{hybr}}\|$	$\|\mathbf{z}^{\text{C}}_{\text{num}} - \mathbf{z}^{\text{C}}_{\text{appr}}\|$	$\|\mathbf{z}^{\text{C}}_{\text{num}} - \mathbf{z}^{\text{C}}_{\text{spher}}\|$
Ammonia				
N	47	475	951	35920
H	705	3521	85980	1343000
Epoxide				
O1	5	119	301	51120
C2	1	152	320	18290
H2*a*	131	364	17220	1011000
H2*b*	294	894	17990	1131000
C3	7	290	1154	33400
H3*a*	519	1813	50850	1344000
H3*b*	191	863	26680	1238000
L-Alanine				
N1	5	127	313	8932
H1*a*	151	869	37230	1076000
H1*b*	149	192	17360	929600
H1*c*	166	1116	48640	774200
C1	2	77	71	26240
H1	170	687	22420	904900
C2	1	62	193	2788
H2*a*	144	236	19900	1114000
H2*b*	64	146	20740	1281000
H2*c*	133	457	13590	865500
C3	1	118	75	7201
O1	1	103	255	20220
O2	2	146	213	8635

4.2. Atomic positions

In Table 4, we compare the individual atom positions, where $\mathbf{z}^{\text{C}}_{*}$ denotes the three Cartesian positional coordinates of the chosen atom, at the final model obtained through the corresponding refinement with $* \in \{\text{num, appr, hybr, spher}\}$. We compare each final model against the final model $\mathbf{x}_{\text{num}}$.

In both spherical and approximate non-spherical refinement, the H atoms are significantly further from the positions

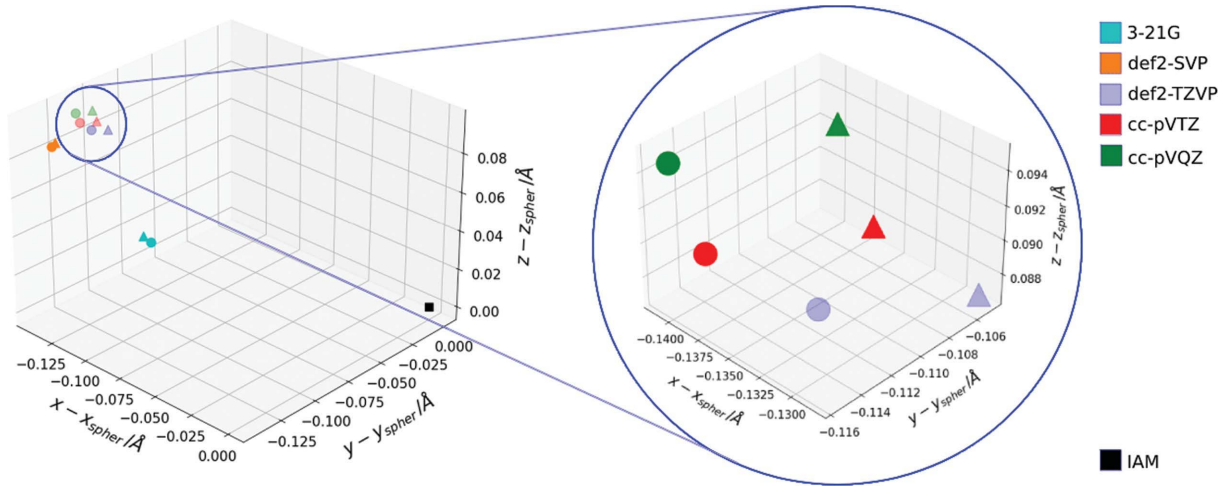

Figure 8
The position of the H atom (in Å), obtained through classical spherical refinement (black square) and non-spherical refinement processes (approximate = triangles and numerical = circles) using various basis sets, where the H atom in the classical spherical model is shifted to the origin (0,0,0). The integration accuracy used is 'Normal' (ammonia).

at $\mathbf{x}_{\rm num}$ than heavier atoms are. This difference is dramatically reduced in the case of hybrid non-spherical refinement.

Table 4 also demonstrates that approximate non-spherical refinement provides an agreement with numerical non-spherical refinement which is 100-fold better than spherical refinement is. Hybrid refinement then further provides a 20- to 50-fold better agreement for the H atoms.

This shows that there is a significant change from spherical to approximate non-spherical refinement, and a further change from approximate to hybrid non-spherical refinement with regards to the H-atom positions in the direction of numerical non-spherical refinement.

4.3. Basis-set dependence

When utilizing quantum-mechanical calculations, the user needs to select a method, a basis set, and also needs to utilize an accuracy for the integration grids, which can be selected from the pre-defined settings 'High', 'Normal' and 'Low' in *NoSpherA2*.

We carried out refinement procedures with the method of PBE with five basis sets for ammonia – 3-21G, def2-SVP, def2-TZVP, cc-pVTZ, cc-pVQZ [for details on these basis sets, see Pritchard *et al.* (2019)] – and our results are shown in Fig. 8.

In Fig. 8 we compare the H positions of the results using various options for the basis sets in three-dimensional space. Fig. 8 clearly indicates that the difference between smaller basis sets [3-21G (teal) and def2-SVP (orange)] and larger ones [def2-TZVP (purple), cc-pVTZ (red) and cc-pVQZ (green)] is far more significant than the difference between approximate non-spherical and numerical non-spherical refinements. Additionally, the difference between larger basis sets is roughly of the same magnitude as the change introduced by using numerical rather than approximate non-spherical refinement.

We finally note here that every larger basis set results in an additional movement in the $-y$ direction when numerical non-spherical refinement is used instead of approximate non-spherical refinement. Further details including different integration grids, which had a smaller impact, can be found in the supporting information in Figs. S29 and S30.

5. Bringing in uncertainties

In this section we compare the parameters of corresponding atoms in the models $\mathbf{x}_{\rm num}$, $\mathbf{x}_{\rm appr}$ and $\mathbf{x}_{\rm spher}$ together with their uncertainties. These uncertainties are error measures for the parameters obtained in the least-squares minimization process. They are represented by the variance–covariance matrix of the model $\mathbf{x}$ given by the following rescaling of the inverse of the normal matrix $B(\mathbf{x})$:

$$\mathrm{Var}(\mathbf{x}) = \frac{||\tilde{\mathbf{r}}||_w^2}{\#_{\rm obs} - \#_{\rm param}} B(\mathbf{x})^{-1} \qquad (7)$$

[formula (3.1.10.2) in Shmueli (2010)], where $||\tilde{\mathbf{r}}||_w$ is the weighted norm introduced in (6) of the residual $\tilde{\mathbf{r}}$, $\#_{\rm obs}$ is the number of observations taken into account in the refinement process and $\#_{\rm param}$ is the number of parameters contained in the vectors $\mathbf{x}_{\rm num}$, $\mathbf{x}_{\rm appr}$ and $\mathbf{x}_{\rm spher}$ (that is, their length) [for more information on the normal matrix see (13) in Appendix *A*]. We note that the prefactor $||\tilde{\mathbf{r}}||_w^2/(\#_{\rm obs} - \#_{\rm param})$ coincides with the square of the goodness of fit.

The positional or ADP uncertainties of any atom in any of the final models $\mathbf{x}$ can be extracted from $\mathrm{Var}(\mathbf{x})$ and are represented by 3×3 or 6×6 submatrices, respectively. Through a transformation into Cartesian coordinates and calculations of the eigenvalues of this matrix, we can derive lower and upper bounds of these uncertainties. These bounds can be represented by balls centred at the atom (for the mathematical details see Appendix *B*), and these *inner* and *outer uncertainty balls* can be plotted to allow us to compare corresponding atoms of the different final models with respect to their uncertainties.

The uncertainties are illustrated as follows. In any dimension, three points can be displayed on a single plane. We apply this fact to the atomic positions of corresponding atoms in $\mathbf{x}_{num}$, $\mathbf{x}_{appr}$ and $\mathbf{x}_{spher}$, and include the uncertainty balls for epoxide in Figs. 9 and 10 (equivalent diagrams for L-alanine and ammonia and for uncertainties of ADPs can be found in the supporting information in Figs. S31–S42, alongside Tables S3–S8 of the precise values of these bounds). With regards to the balls we use the following colour code: green balls represent inner uncertainty balls and red balls represent outer uncertainty balls.

Figs. 9 and 10 confirm that each individual atom of $\mathbf{x}_{num}$ and $\mathbf{x}_{appr}$ lies well within each others' uncertainty bounds, whilst the corresponding atom of $\mathbf{x}_{spher}$ lies much further away. While the significant difference in H position between $\mathbf{x}_{spher}$ and $\mathbf{x}_{appr}$ is well known, such a difference often holds true even for non-H atoms (see Fig. 10). Similar phenomena for L-alanine and ammonia are presented in Figs. S31–S32 and S39–S40 in the supporting information. We conclude that there is such a strong agreement between approximate and numerical non-spherical refinement that the simplification of setting (*) in (1) to zero is justified.

6. Conclusions

Over the course of this work, we have obtained the following results:

(i) Numerical non-spherical refinement is robust and mathematically more complete, but the time cost makes it unviable for practical use.

(ii) The best choice for the step size δ in numerical non-spherical refinement is between 10^{-3} and 10^{-2} Å for our choice of molecules, which provides converging and consistent wR_2-reducing results.

(iii) Approximate non-spherical refinement (as currently used in *NoSpherA2* and other non-spherical structural refinement methods) is significantly closer to numerical non-spherical refinement, in terms of wR_2 factor, X—H distances and atomic positions, than spherical refinement is.

(iv) Hybrid non-spherical refinement, which only calculates the H-atom derivatives of the form factor via numerical differentiation, provides a compromised change of the approximate method towards numerical non-spherical refinement. It provides a time-cost reduction roughly equivalent to the proportion of non-H atoms in the model compared with the complete numerical refinement.

(v) We have implemented a framework which can be adapted for similar analysis of other aspects of refinement processes, in contexts where numerical differentiation is required for mathematically accurate computation.

(vi) We have introduced the concept of 'uncertainty balls' for the visualization of relative differences of parameters with regards to their uncertainties.

(vii) Considering the refinement uncertainties, the differences of results from approximate and numerical non-spherical refinement are insignificant for both H and non-H atoms.

The fundamental question of this paper was the impact of assuming the form factor derivatives to be zero during the least-squares refinement process. Our investigations have shown that the impact of this assumption is negligible, and therefore we can be confident in applying it within *NoSpherA2*.

This result is not limited exclusively to Hirshfeld atom refinement and we expect that other non-spherical approaches are also unaffected by this approximation.

7. Outlook

The validation of non-significance of the derivatives of atomic form factors in non-spherical refinements removes one of the concerns about the accuracy of non-spherical structural refinement techniques. This leads to the natural question, whether these techniques provide better agreement with the

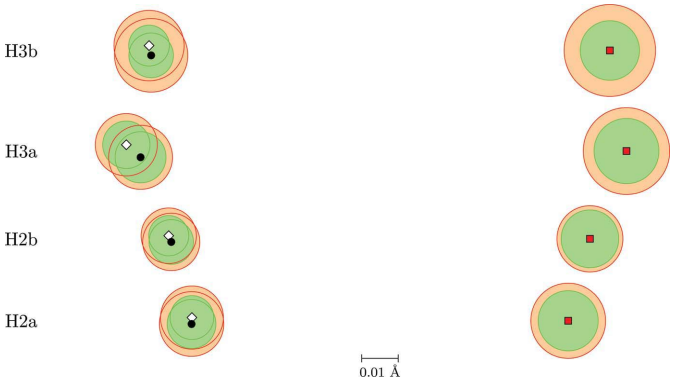

Figure 9
Positions of the H atoms in $\mathbf{x}_{num}$ (white diamond), $\mathbf{x}_{appr}$ (black circle) and $\mathbf{x}_{spher}$ (red square), and their uncertainty balls. Green balls represent inner uncertainty balls and red balls represent outer uncertainty balls (epoxide).

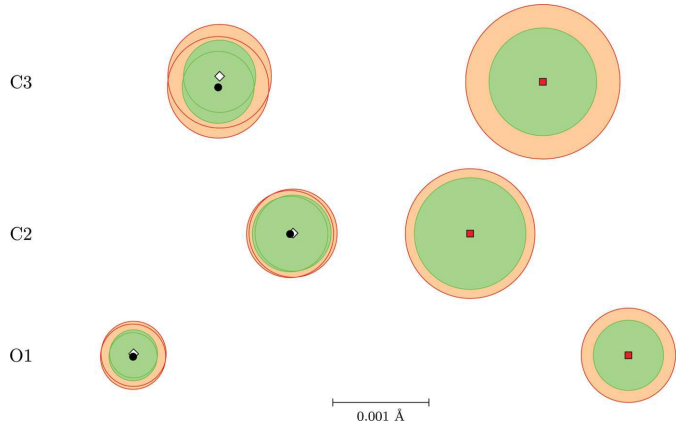

Figure 10
Positions of the non-H atoms in $\mathbf{x}_{num}$ (white diamond), $\mathbf{x}_{appr}$ (black circle) and $\mathbf{x}_{spher}$ (red square), and their uncertainty balls. Green balls represent inner uncertainty balls and red balls represent outer uncertainty balls (epoxide).

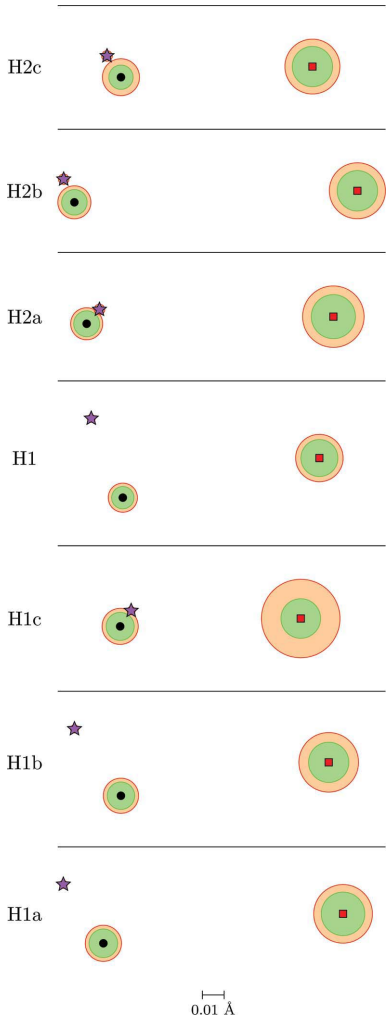

Figure 11
Positions of the H atoms in $\mathbf{x}_{\text{neutron}}$ (purple star), $\mathbf{x}_{\text{appr}}$ (black circle) and $\mathbf{x}_{\text{spher}}$ (red square), and their uncertainty balls. Green balls represent inner uncertainty balls and red balls represent outer uncertainty balls (L-alanine).

structural parameters obtainable by other techniques. Here we want to remind the reader of the already documented (Sanjuan-Szklarz *et al.*, 2020; Fugel *et al.*, 2018; Woińska *et al.*, 2016, 2017; Kleemiss *et al.*, 2021; Malaspina *et al.*, 2019, 2020; Jha *et al.*, 2020; Dittrich *et al.*, 2017; Wieduwilt *et al.*, 2021) improvement of X—H distances obtainable by X-ray diffraction data in comparison with neutron diffraction, which can also be visualized using the techniques presented in this work. In Fig. 11 we show the positions and uncertainty radii of H atoms from the refinements of L-alanine using $\mathbf{x}_{\text{spher}}$ and $\mathbf{x}_{\text{appr}}$ in comparison with $\mathbf{x}_{\text{neutron}}$, taken from Laue diffraction data as reported by Malaspina *et al.* (2019) and already used as a reference by Kleemiss *et al.* (2021). As expected from the previous studies, the H-atom positions in $\mathbf{x}_{\text{appr}}$ are significantly closer to those given by the neutron data. In comparison, their positions in $\mathbf{x}_{\text{spher}}$ are significantly much more distant and less precise. However, even in $\mathbf{x}_{\text{appr}}$ they do remain outside of the corresponding uncertainty balls, showing that the accuracy of the determination of X—H distances from X-ray diffraction is much improved with non-spherical approaches but does not yet equal that of neutron diffraction. The non-H-atom and ADP comparisons can be found in the supporting information (Figs. S43–S46).

APPENDIX *A*
Shift vector computation in the least-squares minimization

In this appendix we discuss the mathematical details of the shift vector computation in the non-spherical refinement processes. While there are similarities to the arguments given in Appendix *B* of Bourhis *et al.* (2015), there are also conceptual differences: we introduce a modified design matrix $\widetilde{D}(\mathbf{x})$ and we distinguish carefully between terms involving only the structure factors themselves and other terms which also require their partial derivatives. This is important since all non-spherical refinement processes rest on the same non-spherical structure factors, but they differ in the computation of their partial derivatives.

A1. Preliminaries

Let Y_{o} be the set of observed intensities corresponding to the Miller indices $\mathbf{h}_1, \ldots, \mathbf{h}_M$ with associated weights $w(\mathbf{h}_m)$, $1 \le m \le M$. We view Y_{o} as a column vector with components $Y_{\text{o}}(\mathbf{h}_m)$. The weights w give rise to a *weighted scalar product* on two such column vectors X, Y given by

$$\langle X, Y\rangle_w = \sum_{m=1}^{M} w(\mathbf{h}_m)X(\mathbf{h}_m)Y(\mathbf{h}_m),$$

and its corresponding weighted norm $\|X\|_w = (\langle X, X\rangle_w)^{1/2}$ [see also (6)].

A given model $\mathbf{x}$ gives rise to a list of non-spherical form factors $f_j(\mathbf{z}, \mathbf{h}_m)$ provided by a tsc file. These form factors determine the structure factor $F_{\text{c}}(\mathbf{x}, \mathbf{h}_m)$ via (1) and the corresponding theoretical intensities $Y_{\text{c}}(\mathbf{x}, \mathbf{h}_m) = |F_{\text{c}}(\mathbf{x}, \mathbf{h}_m)|^2$. We view the set of theoretical intensities again as a column vector $Y_{\text{c}}(\mathbf{x})$.

A2. The residual and the scale factor

The *residual vector* measures the difference between observed and theoretical intensities involving a scale factor $K > 0$:

$$r(\mathbf{x}, K) = Y_{\text{o}} - KY_{\text{c}}(\mathbf{x}).$$

The scale factor is chosen in such a way that $L(\mathbf{x}, K) = \|r(\mathbf{x}, K)\|_w^2$ becomes minimal. Since

$$\begin{aligned} L(\mathbf{x}, K) &= \|Y_{\text{o}}\|_w^2 - 2K\langle Y_{\text{o}}, Y_{\text{c}}(\mathbf{x})\rangle_w + K^2\|Y_{\text{c}}(\mathbf{x})\|_w^2 \\ &= \|Y_{\text{c}}(\mathbf{x})\|_w^2\left[K - \frac{\langle Y_{\text{o}}, Y_{\text{c}}(\mathbf{x})\rangle_w}{\|Y_{\text{c}}(\mathbf{x})\|_w^2}\right]^2 \\ &\quad + \|Y_{\text{o}}\|_w^2 - \frac{\langle Y_{\text{o}}, Y_{\text{c}}(\mathbf{x})\rangle_w^2}{\|Y_{\text{c}}(\mathbf{x})\|_w^2}, \end{aligned}$$

this minimum is attained by the following choice of the scale factor:

$$\widetilde{K} = \widetilde{K}(\mathbf{x}) = \frac{\langle Y_o, Y_c(\mathbf{x})\rangle_w}{\|Y_c(\mathbf{x})\|_w^2}.$$

The residual corresponding to the scale factor $\widetilde{K}$ minimizing $\|r(\mathbf{x}, K)\|_w$ is denoted by $\widetilde{r}(\mathbf{x})$ and given by

$$\widetilde{r}(\mathbf{x}) = Y_o - \widetilde{K}Y_c(\mathbf{x}) = Y_o - \frac{\langle Y_o, Y_c(\mathbf{x})\rangle_w}{\|Y_c(\mathbf{x})\|_w^2} Y_c(\mathbf{x}).$$

Note that the residual $\widetilde{r}$ depends only on the weights and the theoretical and observed intensities and not on the partial derivatives of the theoretical intensities.

A3. Design matrices

The entries of the *design matrix* $D(\mathbf{x})$ are given by

$$[D(\mathbf{x})]_{mn} = \frac{\partial Y_c}{\partial x_n}(\mathbf{x}, \mathbf{h}_m),$$

with $1 \le n \le N$, $1 \le m \le M$ and N is the length of the vector $\mathbf{x}$, that is, the number of refined parameters. Their computation involves the partial derivatives of the structure factor F_c since

$$\frac{\partial Y_c}{\partial x_n}(\mathbf{x}, \mathbf{h}) = 2\mathrm{Re}\left[F_c^*(\mathbf{x}, \mathbf{h})\, \frac{\partial F_c}{\partial x_n}(\mathbf{x}, \mathbf{h})\right],$$

where $F_c^*(\mathbf{x}, \mathbf{h})$ denotes the complex conjugate of $F_c(\mathbf{x}, \mathbf{h})$. The general form of partial derivatives of F_c is given in formula (2).

For x_n representing ADPs, we calculate these partial derivatives analytically:

$$\frac{\partial F_c}{\partial x_n}(\mathbf{x}, \mathbf{h}) = \sum_{j=1}^{N_{\text{atoms}}} f_j(\mathbf{x}, \mathbf{h}) \frac{\partial G_j}{\partial x_n}(\mathbf{x}, \mathbf{h}). \tag{8}$$

In the case of positional parameters x_n, our refinement methods differ. In the case of approximate non-spherical refinement, these partial derivatives are approximated by the expression

$$\frac{\partial F_c}{\partial x_n}(\mathbf{x}, \mathbf{h}) \simeq \sum_{j=1}^{N_{\text{atoms}}} f_j(\mathbf{x}, \mathbf{h}) \frac{\partial G_j}{\partial x_n}(\mathbf{x}, \mathbf{h}). \tag{9}$$

Numerical non-spherical refinement uses the more accurate difference quotients

$$\frac{\partial F_c}{\partial x_n}(\mathbf{x}, \mathbf{h}) \simeq \frac{F_c(\mathbf{x} + \epsilon\mathbf{e}_n, \mathbf{h}) - F_c(\mathbf{x} - \epsilon\mathbf{e}_n, \mathbf{h})}{2\epsilon}. \tag{10}$$

Hybrid non-spherical refinement uses a combination of both choices, namely (9) for partial derivatives in positional directions of heavier atoms and (10) for positional directions of the H atoms [and (8) for all partial derivatives with respect to ADPs].

To have a good fit with the observed intensities Y_o, the rescaled theoretical intensities $\widetilde{K}Y_c$ should be used instead of Y_c, which leads to the following modification $\widetilde{D}(\mathbf{x})$ of the design matrix,

$$[\widetilde{D}(\mathbf{x})]_{mn} = \frac{\partial \widetilde{K}Y_c}{\partial x_n}(\mathbf{x}, \mathbf{h}_m) = \frac{\partial \widetilde{K}}{\partial x_n}(\mathbf{x}) Y_c(\mathbf{x}, \mathbf{h}_m) + \widetilde{K}(\mathbf{x})[D(\mathbf{x})]_{mn},$$

where

$$\frac{\partial \widetilde{K}}{\partial x_n}(\mathbf{x}) = \frac{1}{\|Y_c(\mathbf{x})\|_w^2} \left\langle \frac{\partial Y_c}{\partial x_n}(\mathbf{x}),\, Y_o - 2\widetilde{K}(\mathbf{x})Y_c(\mathbf{x}) \right\rangle_w. \tag{11}$$

The two design matrices are thus related by

$$\widetilde{D}(\mathbf{x}) = \widetilde{K}(\mathbf{x})D(\mathbf{x}) + Y_c(\mathbf{x})\Big[\operatorname{grad} \widetilde{K}(\mathbf{x})\Big]^\top, \tag{12}$$

where $Y_c(\mathbf{x})$ is a column vector and where the gradient $\operatorname{grad} f$ of a function $f : \mathbb{R}^N \to \mathbb{R}$ is the column vector of the partial derivatives $\partial f/\partial x_n$. The design matrix $\widetilde{D}(\mathbf{x})$ is therefore a rank-one perturbation of the product $\widetilde{K}(\mathbf{x})D(\mathbf{x})$. Its computation requires the structure factor F_c together with its partial derivatives $\partial F_c/\partial x_n$.

A4. Shift vector computation

The two ingredients of the shift vector computation are the residual $\widetilde{r}(\mathbf{x})$ and the design matrix $\widetilde{D}(\mathbf{x})$. While the residual only requires the structure factor itself and is the same for all non-spherical refinement processes, the computation of the design matrix is different for each of the non-spherical refinement processes. The computation of $\widetilde{D}(\mathbf{x})$ via numerical differentiation in the case of numerical non-spherical refinement is much more time consuming since it relies on two further quantum-mechanical computations for each partial derivative in positional directions. Hybrid non-spherical refinement is a compromise providing near-identical results (to numerical non-spherical refinement) for the final model by only computing derivatives of the H atoms via numerical differentiation and thus reducing the overall computation time.

The *normal matrix* $B(\mathbf{x})$ is the symmetric matrix

$$B(\mathbf{x}) = \widetilde{D}(\mathbf{x})^\top W \widetilde{D}(\mathbf{x}), \tag{13}$$

where W is the $M \times M$ diagonal matrix with the weights $w(\mathbf{h}_m)$ on the diagonal. In the standard case of the Gauss–Newton method, the *shift vector* $s(\mathbf{x})$ is then computed via the formula [see also (72) of Bourhis *et al.* (2015)]

$$B(\mathbf{x})s(\mathbf{x}) = \widetilde{D}(\mathbf{x})^\top W \widetilde{r}(\mathbf{x}). \tag{14}$$

The derivation of the shift $s(\mathbf{x})$ on the left-hand side of this equation is carried out utilizing the Cholesky decomposition of $B(\mathbf{x})$. The new model is then given by $\mathbf{x} + s(\mathbf{x})$. This completes the mathematical description of an iteration step in the least-squares minimization.

APPENDIX *B*
Uncertainty balls

In this appendix we provide the mathematical justification for the use of inner and outer uncertainty balls of the positional parameters of a specific atomic site (or of its ADPs) and explain how these balls and their radii are calculated.

In our derivation we will make repeated use of the following fundamental rule [see, *e.g.*, III.5 in Feller (1971)]: if random vectors $\mathbf{x}$ and $\mathbf{y}$ are transformed via $\mathbf{y} = A\mathbf{x} + \mathbf{b}$ (with a fixed matrix A and a fixed vector $\mathbf{b}$) then their corresponding variance–covariance matrices are related by

$$\mathrm{Var}(\mathbf{y}) = A\,\mathrm{Var}(\mathbf{x})\,A^{\top}. \tag{15}$$

The first transformation from the vector $\mathbf{x}$ (representing a model) into the crystallographic parameters $\mathbf{y}$ is often the identity (in the case of epoxide and L-alanine), but in other cases with constraints (like ammonia) the expansion may be given by some matrix J, that is $\mathbf{y} = J\mathbf{x}$ [the choice of J for ammonia can be found in the supporting information in equation (S1)]. Application of the above rule yields $\mathrm{Var}(\mathbf{y}) = J\,\mathrm{Var}(\mathbf{x})\,J^{\top}$ [see also (35) of Bourhis *et al.* (2015)].

The variance–covariance matrix of the fractional positional coordinates $\mathbf{z}$ of an atom is a specific 3×3 submatrix of $\mathrm{Var}(\mathbf{y})$. The transformation to Cartesian coordinates is given through multiplication with the orthogonalization matrix A, that is, $\mathbf{z}^{\mathrm{C}} = A\mathbf{z}$. Consequently, the above rule yields $\mathrm{Var}(\mathbf{z}^{\mathrm{C}}) = A\,\mathrm{Var}(\mathbf{z})\,A^{\top}$.

For the ADPs of an atom, we utilize the matrix

$$U^{*} = \begin{bmatrix} U^{*}_{11} & U^{*}_{12} & U^{*}_{13} \\ U^{*}_{12} & U^{*}_{22} & U^{*}_{23} \\ U^{*}_{13} & U^{*}_{23} & U^{*}_{33} \end{bmatrix}$$

[U^{*} is the unitless representation of the ADPs as in Grosse-Kunstleve & Adams (2002)] and transform it with the help of the orthogonalization matrix A into a Cartesian matrix:

$$U^{\mathrm{C}} = \begin{bmatrix} U^{\mathrm{C}}_{11} & U^{\mathrm{C}}_{12} & U^{\mathrm{C}}_{13} \\ U^{\mathrm{C}}_{12} & U^{\mathrm{C}}_{22} & U^{\mathrm{C}}_{23} \\ U^{\mathrm{C}}_{13} & U^{\mathrm{C}}_{23} & U^{\mathrm{C}}_{33} \end{bmatrix} = A \begin{bmatrix} U^{*}_{11} & U^{*}_{12} & U^{*}_{13} \\ U^{*}_{12} & U^{*}_{22} & U^{*}_{23} \\ U^{*}_{13} & U^{*}_{23} & U^{*}_{33} \end{bmatrix} A^{\top}. \tag{16}$$

This transformation can be equivalently written as

$$\begin{aligned} &\begin{bmatrix} U^{\mathrm{C}}_{11} & U^{\mathrm{C}}_{22} & U^{\mathrm{C}}_{33} & U^{\mathrm{C}}_{12} & U^{\mathrm{C}}_{13} & U^{\mathrm{C}}_{23} \end{bmatrix}^{\top} \\ &= B \begin{bmatrix} U^{*}_{11} & U^{*}_{22} & U^{*}_{33} & U^{*}_{12} & U^{*}_{13} & U^{*}_{23} \end{bmatrix}^{\top} \end{aligned} \tag{17}$$

with a suitably chosen 6×6 matrix B, which can then be used with the above rule to obtain $\mathrm{Var}(U^{\mathrm{C}})$ [see Parois & Lutz (2011) for further details].

The uncertainty of the random vector $\mathbf{z}^{\mathrm{C}}$ *in direction* $\mathbf{v}$ is given by the expression

$$\left[\sigma_{\mathbf{v}}(\mathbf{z}^{\mathrm{C}})\right]^2 = \frac{\mathbf{v}^{\top}\,\mathrm{Var}(\mathbf{z}^{\mathrm{C}})\,\mathbf{v}}{\mathbf{v}^{\top}\mathbf{v}}. \tag{18}$$

We postpone the derivation of (18) and first discuss its usage. If the random parameters $\mathbf{z}^{\mathrm{C}}$ are restricted by certain constraints (as in the case of ammonia), we only consider admissible directions complying with these constraints, and we define the inner and outer uncertainty radii as the smallest and largest uncertainties appearing in all admissible directions.

The fraction on the right-hand side of (18) is known as Rayleigh's quotient [see *e.g.* p. 176 of Horn & Johnson (2013)], and is bounded by the maximal and minimal eigenvalues of the symmetric and positive semidefinite matrix $\mathrm{Var}(\mathbf{z}^{\mathrm{C}})$.

In the case of constraints, the uncertainty in any direction $\mathbf{v}$ perpendicular to the subspace of admissible directions is identically zero, that is, $\mathbf{v}$ lies in the kernel of $\mathrm{Var}(\mathbf{z}^{\mathrm{C}})$. If $\mathbf{v}$ is an admissible direction, the uncertainty $\sigma_{\mathbf{v}}(\mathbf{z}^{\mathrm{C}})$ in direction $\mathbf{v}$ lies in the interval $[(\lambda_{\min})^{1/2}, (\lambda_{\max})^{1/2}]$, where $\lambda_{\min}$ and $\lambda_{\max}$ are the smallest and the largest non-zero eigenvalue of the positive semidefinite matrix $\mathrm{Var}(\mathbf{z}^{\mathrm{C}})$. Consequently, the uncertainties in any admissible direction are sandwiched between the balls with radii $(\lambda_{\min})^{1/2}$ and $(\lambda_{\max})^{1/2}$. We call these balls the *inner* and *outer uncertainty balls* of $\mathbf{z}^{\mathrm{C}}$. These uncertainty balls are displayed as red and green balls on Figs. 9, 10 and 11. Analogous considerations can be carried out for the ADPs of an atom, viewed as a random vector in $\mathbb{R}^6$.

Let us finally return to formula (18) and its derivation. The specific direction $\mathbf{v} \in \mathbb{R}^3$ determines a Euclidean line $\ell = \mathbb{R} \cdot \mathbf{v}_0$, where $\mathbf{v}_0 = \mathbf{v}/\|\mathbf{v}\|$ is the unit vector corresponding to $\mathbf{v}$. The orthogonal projection of the random vector $\mathbf{z}^{\mathrm{C}}$ onto this line is given by the inner product $\mathbf{v}_0 \cdot \mathbf{z}^{\mathrm{C}} = \|\mathbf{z}^{\mathrm{C}}\| \cos\alpha$, where α is the angle between $\mathbf{z}^{\mathrm{C}}$ and $\mathbf{v}_0$. This orthogonal projection of $\mathbf{z}^{\mathrm{C}}$ onto the line ℓ is a new one-dimensional random variable, and we refer to its variance (and its uncertainty) as the variance (and uncertainty) of the random vector $\mathbf{z}^{\mathrm{C}}$ in direction $\mathbf{v}$. Rewriting the inner product as the matrix-vector multiplication $\mathbf{v}_0^{\top}\mathbf{z}^{\mathrm{C}}$ and applying (15) (with $A = \mathbf{v}_0^{\top}$ and $\mathbf{b} = 0$) we obtain

$$\left[\sigma_{\mathbf{v}}(\mathbf{z}^{\mathrm{C}})\right]^2 = \mathrm{Var}(\mathbf{v}_0^{\top}\mathbf{z}^{\mathrm{C}}) = \mathbf{v}_0^{\top}\,\mathrm{Var}(\mathbf{z}^{\mathrm{C}})\,\mathbf{v}_0 = \frac{\mathbf{v}^{\top}\,\mathrm{Var}(\mathbf{z}^{\mathrm{C}})\,\mathbf{v}}{\mathbf{v}^{\top}\mathbf{v}}.$$

This completes our mathematical discussion of the uncertainties of positional parameters and ADPs of specific atoms and their associated uncertainty balls.

Funding information

Funding for this research was provided by: European Regional Development Fund (grant No. 25R17P01847 to Laura Midgley).

References

Bąk, J. M., Domagała, S., Hübschle, C., Jelsch, C., Dittrich, B. & Dominiak, P. M. (2011). *Acta Cryst.* A**67**, 141–153.
Boese, R., Niederprüm, N., Bläser, D., Maulitz, A., Antipin, M. Y. & Mallinson, P. R. (1997). *J. Phys. Chem. B*, **101**, 5794–5799.
Bourhis, L. J., Dolomanov, O. V., Gildea, R. J., Howard, J. A. K. & Puschmann, H. (2015). *Acta Cryst.* A**71**, 59–75.
Capelli, S. C., Bürgi, H.-B., Dittrich, B., Grabowsky, S. & Jayatilaka, D. (2014). *IUCrJ*, **1**, 361–379.
Chodkiewicz, M. L., Migacz, S., Rudnicki, W., Makal, A., Kalinowski, J. A., Moriarty, N. W., Grosse-Kunstleve, R. W., Afonine, P. V., Adams, P. D. & Dominiak, P. M. (2018). *J. Appl. Cryst.* **51**, 193–199.
Chodkiewicz, M. L., Woińska, M. & Woźniak, K. (2020). *IUCrJ*, **7**, 1199–1215.
Compton, A. H. (1915). *Nature*, **95**, 343–344.
Coppens, P. (1967). *Science*, **158**, 1577–1579.
Debye, P. (1915). *Ann. Phys.* **351**, 809–823.
Destro, R., Marsh, R. E. & Bianchi, R. (1988). *J. Phys. Chem.* **92**, 966–973.
Dittrich, B., Hübschle, C. B., Luger, P. & Spackman, M. A. (2006). *Acta Cryst.* D**62**, 1325–1335.
Dittrich, B., Lübben, J., Mebs, S., Wagner, A., Luger, P. & Flaig, R. (2017). *Chem. Eur. J.* **23**, 4605–4614.

Dolomanov, O. V., Bourhis, L. J., Gildea, R. J., Howard, J. A. K. & Puschmann, H. (2009). *J. Appl. Cryst.* **42**, 339–341.
Domagała, S., Fournier, B., Liebschner, D., Guillot, B. & Jelsch, C. (2012). *Acta Cryst.* A**68**, 337–351.
Feller, W. (1971). *An Introduction to Probability Theory and its Applications*, Vol. II, 2nd ed. New York: John Wiley & Sons, Inc.
Fugel, M., Jayatilaka, D., Hupf, E., Overgaard, J., Hathwar, V. R., Macchi, P., Turner, M. J., Howard, J. A. K., Dolomanov, O. V., Puschmann, H., Iversen, B. B., Bürgi, H.-B. & Grabowsky, S. (2018). *IUCrJ*, **5**, 32–44.
Genoni, A., Bučinský, L., Claiser, N., Contreras–García, J., Dittrich, B., Dominiak, P. M., Espinosa, E., Gatti, C., Giannozzi, P., Gillet, J.-M., Jayatilaka, D., Macchi, P., Madsen, A. O., Massa, L., Matta, C. F., Merz, K. M. Jr, Nakashima, P. N. H., Ott, H., Ryde, U., Schwarz, K., Sierka, M. & Grabowsky, S. (2018). *Chem. Eur. J.* **24**, 10881–10905.
Genoni, A. & Macchi, P. (2020). *Crystals*, **10**, 473.
Gildea, R. J., Bourhis, L. J., Dolomanov, O. V., Grosse-Kunstleve, R. W., Puschmann, H., Adams, P. D. & Howard, J. A. K. (2011). *J. Appl. Cryst.* **44**, 1259–1263.
Grabowsky, S., Genoni, A. & Bürgi, H.-B. (2017). *Chem. Sci.* **8**, 4159–4176.
Grabowsky, S., Jayatilaka, D., Mebs, S. & Luger, P. (2010). *Chem. Eur. J.* **16**, 12818–12821.
Grabowsky, S., Weber, M., Buschmann, J. & Luger, P. (2008). *Acta Cryst.* B**64**, 397–400.
Grosse-Kunstleve, R. W. & Adams, P. D. (2002). *J. Appl. Cryst.* **35**, 477–480.
Hansen, N. K. & Coppens, P. (1978). *Acta Cryst.* A**34**, 909–921.
Hirshfeld, F. L. (1977). *Theor. Chim. Acta*, **44**, 129–138.
Horn, R. A. & Johnson, C. R. (2013). *Matrix Analysis*, 2nd ed. Cambridge University Press.
Jarzembska, K. N. & Dominiak, P. M. (2012). *Acta Cryst.* A**68**, 139–147.
Jayatilaka, D. & Dittrich, B. (2008). *Acta Cryst.* A**64**, 383–393.
Jha, K. K., Gruza, B., Kumar, P., Chodkiewicz, M. L. & Dominiak, P. M. (2020). *Acta Cryst.* B**76**, 296–306.
Kleemiss, F., Dolomanov, O. V., Bodensteiner, M., Peyerimhoff, N., Midgley, L., Bourhis, L. J., Genoni, A., Malaspina, L. A., Jayatilaka, D., Spencer, J. L., White, F., Grundkötter-Stock, B., Steinhauer, S., Lentz, D., Puschmann, H. & Grabowsky, S. (2021). *Chem. Sci.* **12**, 1675–1692.
Koritsanszky, T. S. & Coppens, P. (2001). *Chem. Rev.* **101**, 1583–1628.
Kumar, P., Gruza, B., Bojarowski, S. A. & Dominiak, P. M. (2019). *Acta Cryst.* A**75**, 398–408.
Macchi, P. (2020). *Crystallogr. Rev.* **26**, 209–268.
Malaspina, L. A., Hoser, A. A., Edwards, A. J., Woińska, M., Turner, M. J., Price, J. R., Sugimoto, K., Nishibori, E., Bürgi, H.-B., Jayatilaka, D. & Grabowsky, S. (2020). *CrystEngComm*, **22**, 4778–4789.
Malaspina, L. A., Wieduwilt, E. K., Bergmann, J., Kleemiss, F., Meyer, B., Ruiz-López, M. F., Pal, R., Hupf, E., Beckmann, J., Piltz, R. O., Edwards, A. J., Grabowsky, S. & Genoni, A. (2019). *J. Phys. Chem. Lett.* **10**, 6973–6982.
Midgley, L., Bourhis, L. J., Dolomanov, O., Peyerimhoff, N. & Puschmann, H. (2019). arXiv:1911.08847.
Neese, F. (2012). *WIREs Comput. Mol. Sci.* **2**, 73–78.
Neese, F. (2018). *WIREs Comput. Mol. Sci.* **8**, e1327.
Parois, P. & Lutz, M. (2011). *Acta Cryst.* A**67**, 383–390.
Pritchard, B. P., Altarawy, D., Didier, B., Gibson, T. D. & Windus, T. L. (2019). *J. Chem. Inf. Model.* **59**, 4814–4820.
Sanjuan-Szklarz, W. F., Woińska, M., Domagała, S., Dominiak, P. M., Grabowsky, S., Jayatilaka, D., Gutmann, M. & Woźniak, K. (2020). *IUCrJ*, **7**, 920–933.
Shmueli, U. (2010). Editor. *International Tables for Crystallography*, Vol. B, *Reciprocal Space*. Chester: International Union of Crystallography.
Stewart, R. F. (1977). *Isr. J. Chem.* **16**, 124–131.
Wieduwilt, E. K., Macetti, G. & Genoni, A. (2021). *J. Phys. Chem. Lett.* **12**, 463–471.
Woińska, M., Grabowsky, S., Dominiak, P. M., Woźniak, K. & Jayatilaka, D. (2016). *Sci. Adv.* **2**, e1600192.
Woińska, M., Jayatilaka, D., Dittrich, B., Flaig, R., Luger, P., Woźniak, K., Dominiak, P. M. & Grabowsky, S. (2017). *ChemPhysChem*, **18**, 3334–3351.